

## Radar and optical observations and physical modeling of triple near-Earth Asteroid (136617) 1994 CC

Marina Brozović<sup>a,\*</sup>, Lance A.M. Benner<sup>a</sup>, Patrick A. Taylor<sup>b</sup>, Michael C. Nolan<sup>b</sup>, Ellen S. Howell<sup>b</sup>, Christopher Magri<sup>c</sup>, Daniel J. Scheeres<sup>d</sup>, Jon D. Giorgini<sup>a</sup>, Joseph T. Pollock<sup>e</sup>, Petr Pravec<sup>f</sup>, Adrián Galád<sup>f,g</sup>, Julia Fang<sup>h</sup>, Jean-Luc Margot<sup>h,i</sup>, Michael W. Busch<sup>i</sup>, Michael K. Shepard<sup>j</sup>, Daniel E. Reichart<sup>k</sup>, Kevin M. Ivarsen<sup>k</sup>, Joshua B. Haislip<sup>k</sup>, Aaron P. LaCluyze<sup>k</sup>, Joseph Jao<sup>a</sup>, Martin A. Slade<sup>a</sup>, Kenneth J. Lawrence<sup>a</sup>, Michael D. Hicks<sup>a</sup>

<sup>a</sup>Jet Propulsion Laboratory, California Institute of Technology, Pasadena, CA 91109-8099, USA

<sup>b</sup>Arecibo Observatory, National Astronomy and Ionosphere Center, Arecibo, PR 00612, USA

<sup>c</sup>University of Maine at Farmington, Preble Hall, Farmington, ME 04938, USA

<sup>d</sup>Aerospace Engineering Sciences, University of Colorado, Boulder, CO 80309-0429, USA

<sup>e</sup>Physics and Astronomy Department, Appalachian State University, Boone, NC 28607-4688, USA

<sup>f</sup>Astronomical Institute, Academy of Sciences of the Czech Republic, CZ-25165 Ondřejov, Czech Republic

<sup>g</sup>Modra Observatory, Department of Astronomy, Physics of the Earth, and Meteorology, FMFI UK, Bratislava SK-84248, Slovakia

<sup>h</sup>Department of Physics & Astronomy, University of California, Los Angeles, CA 90095-1567, USA

<sup>i</sup>Department of Earth & Space Sciences, University of California, Los Angeles, CA 90095-1567, USA

<sup>j</sup>Department of Geography & Geosciences, Bloomsburg University, Bloomsburg, PA 17815-1301, USA

<sup>k</sup>Physics and Astronomy Department, University of North Carolina, Chapel Hill, NC 27599-6134, USA

### ARTICLE INFO

#### Article history:

Received 13 May 2011

Revised 29 August 2011

Accepted 1 September 2011

Available online 12 September 2011

#### Keywords:

Asteroids

Near-Earth objects

Radar observations

Satellites of asteroids

### ABSTRACT

We report radar, photometric, and spectroscopic observations of near-Earth Asteroid (136617) 1994 CC. The radar measurements were obtained at Goldstone (8560 MHz, 3.5 cm) and Arecibo (2380 MHz, 12.6 cm) on 9 days following the asteroid's approach within 0.0168 AU on June 10, 2009. 1994 CC was also observed with the Panchromatic Robotic Optical Monitoring and Polarimetry Telescopes (PROMPT) on May 21 and June 1–3. Visible-wavelength spectroscopy was obtained with the 5-m Hale telescope at Palomar on August 25. Delay-Doppler radar images reveal that 1994 CC is a triple system; along with (153591) 2001 SN263, this is only the second confirmed triple in the near-Earth population. Photometry obtained with PROMPT yields a rotation period for the primary  $P = 2.38860 \pm 0.00009$  h and a lightcurve amplitude of  $\sim 0.1$  mag suggesting a shape with low elongation. Hale telescope spectroscopy indicates that 1994 CC is an Sq-class object. Delay-Doppler radar images and shape modeling reveal that the primary has an effective diameter of  $0.62 \pm 0.06$  km, low pole-on elongation, few obvious surface features, and a prominent equatorial ridge and sloped hemispheres that closely resemble those seen on the primary of binary near-Earth Asteroid (66391) 1999 KW4. Detailed orbit fitting reported separately by Fang et al. (Fang, J., Margot, J.-L., Brozovic, M., Nolan, M.C., Benner, L.A.M., Taylor, P.A. [2011]. *Astron. J.* 141, 154–168) gives a mass of the primary of  $2.6 \times 10^{11}$  kg that, coupled with the effective diameter, yields a bulk density of  $2.1 \pm 0.6$  g cm<sup>-3</sup>. The images constrain the diameters of the inner and outer satellites to be  $113 \pm 30$  m and  $80 \pm 30$  m, respectively. The inner satellite has a semimajor axis of  $\sim 1.7$  km ( $\sim 5.5$  primary radii), an orbital period of  $\sim 30$  h, and its Doppler dispersion suggests relatively slow rotation,  $26 \pm 12$  h, consistent with spin-orbit lock. The outer satellite has an orbital period of  $\sim 9$  days and a rotation period of  $14 \pm 7$  h, establishing that the rotation is not spin-orbit locked. Among all binary and triple systems observed by radar, at least 25% (7/28) have a satellite that rotates more rapidly than its orbital period. This suggests that asynchronous configurations with  $P_{\text{rotation}} < P_{\text{orbital}}$  are relatively common among multiple systems in the near-Earth population. 1994 CC's outer satellite has an observed maximum separation from the primary of  $\sim 5.7$  km ( $\sim 18.4$  primary radii) that is the largest separation relative to primary radius seen to date among all 36 known binary and triple NEA systems. 1994 CC, (153591) 2001 SN263, and 1998 ST27 are the only triple and binary systems known with satellite

\* Corresponding author. Address: Mail Stop 301-121, Jet Propulsion Laboratory, California Institute of Technology, Pasadena, CA 91109-8099, USA. Fax: +1 818 393 7116.

E-mail address: [Marina.Brozovic@jpl.nasa.gov](mailto:Marina.Brozovic@jpl.nasa.gov) (M. Brozović).

separations >10 primary radii, suggesting either a detection bias, or that such widely-separated satellites are relatively uncommon in NEA multiple systems.

© 2011 Elsevier Inc. All rights reserved.

## 1. Introduction

Apollo Asteroid (136617) 1994 CC was discovered by Spacewatch on February 3, 1994 and is classified as a “Potentially Hazardous Asteroid” by the Minor Planet Center. On June 10, 2009, 1994 CC approached within 0.0168 AU (6.6 lunar distances, or LD), the closest encounter by this asteroid for at least several hundred years. Prior to the 2009 flyby, nothing was known about this object other than its absolute magnitude of 17.6, which suggested a diameter within a factor of two of 0.9 km. Among all known NEAs with absolute magnitudes brighter than 18, 1994 CC’s flyby was the third closest known well in advance in the last century; only 4179 Toutatis (4.0 LD in 2004) and (33342) 1998 WT24 (4.9 LD in 2001) approached more closely.

We observed 1994 CC with the Goldstone and Arecibo planetary radars and obtained photometry with three of the 0.41-m Panchromatic Robotic Monitoring and Polarimetry Telescopes (PROMPT) in Chile. We also acquired visible wavelength spectroscopy with the 5-m Hale telescope at Palomar. Here, we report radar imaging that reveals 1994 CC is a triple system. Following (153591) 2001 SN263 (Nolan et al., 2008), this is only the second triple system discovered to date in the near-Earth population.

## 2. Observations and data reduction

### 2.1. Lightcurves

We obtained photometry with PROMPT on four nights between May 21 and June 3 (Table 1, data in the Supplementary online material). The raw images were reduced using the photometry program MIRA, which was also used to carry out aperture photometry on the calibrated images. We used dark, bias, and flat field frames in calibration.

Fig. 1 shows lightcurves obtained on May 21 and June 1–3 with the individual Fourier fits (Harris et al., 1989; Harris and Lupishko, 1989) superimposed. The amplitude of the lightcurves is <0.1 mag, suggesting a shape with low elongation. The lightcurve fit was different on each of the four nights. Some of the changes may be due to the presence of satellites, possibly also their rotational components, but some may be due to changing aspect and phase angle. It is worth noting that on June 3, the asteroid was within 40° of the Moon that was 80% full. The available data are insufficient in amount to confirm the presence of satellites, let alone separate the individual lightcurve components, thus we fitted just the dominant component of the lightcurve, which is the primary’s rotation, with a single-period Fourier series. We obtained the rotation period for the primary:  $P = 2.3886 \pm 0.0001$  h. Although similar to the

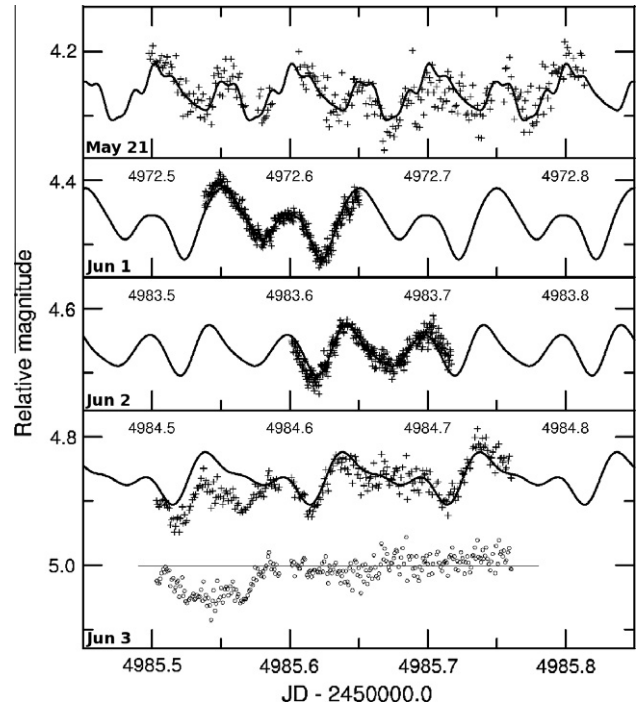


**Fig. 1.** 1994 CC lightcurves obtained at PROMPT on May 21 and June 1–3. A solid black line marks the Fourier series fit that was used to estimate the period. The June 3 lightcurve also contains a candidate mutual event that is suggested by the residuals of the fit (bottom panel).

synodic period, the lightcurve period is different in the sense that it depends on the illumination of the asteroid by the Sun, and because the illumination conditions change as the asteroid moves in its orbit. This is particularly significant for asteroids on close approaches to Earth that move very quickly across the sky.

On June 3 the lightcurves hint that we may have seen a mutual event with an attenuation of  $\sim 0.05$  magnitude centered at 00:58 UT, which was at the beginning of the observations. The data are rather limited (both in quality and quantity), which precludes us from confirming that this actually was a mutual event.

### 2.2. Optical spectrum

We obtained long-slit CCD spectroscopy of 1994 CC on August 25 2009 using the Palomar 5-m Hale telescope equipped with the facility dual-channel spectrometer. Eleven 300 s integrations

**Table 1**  
Photometric observations.

Date	Time range (UTC) Start–Stop	Telescope	Filter	Exposure (s)	RA (°)	Dec (°)	Distance (AU)	S–T–O angle (°)
May 21	00:00–07:30	Prompt3	Red	80	202	–39	0.099	33
June 1	00:54–03:36	Prompt5	R	20	187	–44	0.047	53
June 2	02:25–05:12	Prompt5	R	20	184	–45	0.042	56
June 3	01:48–06:14	Prompt2	Lum	20	180	–46	0.038	59

Masterlog of 1994 CC photometric observations. All observing dates refer to 2009. Right ascension, declination, distance in AU, and Sun–Target–Observer angle are given for the middle of each observing session. We also list the telescope and the filter used, as well as the exposure time for each of the frames. Filter R is a Johnson R-band filter, filter Red is used in RGB color imaging, and filter Lum (Luminance) is a clear filter that blocks the infra-red.

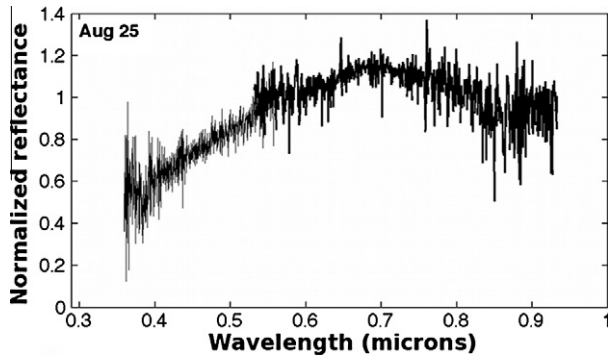


**Fig. 2.** Normalized reflectance obtained at the Palomar 5-m telescope on August 25. A thin black line shows the data taken with the B-filter, while a thick black line shows the data taken with the R-filter.

on the asteroid plus extensive observations of solar analog stars 112–1333, 93–110, 110–361, and 114–654 were used to generate the composite normalized reflectance spectrum shown in Fig. 2. This rotationally-averaged spectrum spans the wavelength range from 0.36 to 0.93  $\mu\text{m}$ . A comparison of our optical spectrum with the 1341 asteroid spectra archived in the SMASS II database (Bus and Binzel, 2002) allowed us to identify 1994 CC as an Sq-type asteroid. An independent study by V. Reddy (personal communication) also found that visible and infrared spectroscopy indicates

that 1994 CC has a silicate-rich mineralogy. The Sq-class is most similar to LL ordinary chondrite meteorites (Binzel et al., 2009).

### 2.3. Radar

1994 CC's close flyby in 2009 presented an outstanding opportunity for radar imaging. We started observing on June 12 at Goldstone, two days after the closest approach, when 1994 CC reached a declination of  $-12^\circ$  and was still only 8 lunar distances away. Observations at Arecibo started on June 13. Table 2 summarizes the observations. Observations at both Goldstone and Arecibo achieved signal-to-noise ratios (SNRs) of several hundred per run, even though equipment problems at Arecibo reduced the transmitter power to only  $\sim 60$  kW, more than an order of magnitude less than Arecibo's nominal transmitter power.

Radar observations involve transmission of a circularly polarized signal and reception of echoes in the same and opposite senses of circular polarization (SC and OC). The circular polarization ratio (SC/OC) provides a measure of the target's near-surface roughness. Small ratios indicate smoothness within an order of magnitude of the radar wavelength while larger ratios indicate significant surface and near-surface roughness. The duration of each transmit–receive cycle (or “run”) is determined by the target's distance. Each run can be analyzed as a sum of some number of statistically independent measurements or “looks”,  $N_{\text{looks}}$ . The data from different looks are combined into incoherent sums in order to reduce the fractional noise fluctuation by  $\sqrt{N_{\text{looks}}}$ . Our observa-

**Table 2**  
Radar observations.

Date	Time range (UTC) Start–Stop	Setup	Resolution		Code	spb	Runs	RA ( $^\circ$ )	Dec ( $^\circ$ )	Distance (AU)	Sol
			( $\mu\text{s}$ )	(Hz)							
<i>Goldstone</i>											
June 12	15:25:49–15:37:19	CW	–	0.98	–	–	17	72	–7	0.020	43
	15:39:19–15:44:34	CW	–	0.98	–	–	8				45
	16:06:17–16:07:14	Ranging	10.0	12.30	127	1	2				45
	16:17:35–16:18:32	Ranging	11.0	11.18	127	1	2				45
	16:35:36–16:44:58	Imaging	0.125	0.50	255	1	14				45
	16:50:28–18:35:00	Imaging	0.125	0.50	255	1	150				47
June 14	13:52:25–14:01:16	CW	–	0.98	–	–	10	60	+6	0.027	49
	14:21:59–14:24:13	Ranging	1.0	7.64	1023	1	3				49
	14:37:32–14:38:50	Ranging	1.0	5.11	255	1	2				49
	14:53:14–17:14:35	Imaging	0.25	0.50	127	1	152				49
June 21	11:31:04–12:30:07	CW	–	0.98	–	–	31	45	+22	0.057	52
	15:44:17–16:44:11	Ranging	1.0	1.91	255	1	31				52
<i>Arecibo</i>											
June 13	15:05:35–15:15:39	CW	–	0.20	–	–	13	65	+1	0.023	49
	15:17:45–15:58:49	Imaging	0.05	0.40	65535	1	52				49
June 14	13:52:18–14:02:42	CW	–	0.20	–	–	12	65	+6	0.027	49
	14:08:00–14:41:37	Imaging	0.5	0.24	8191	1	38				49
	14:44:42–15:59:30	Imaging	0.2	0.20	65535	4	82				49
June 15	13:27:09–13:38:02	CW	–	0.20	–	–	11	56	+11	0.031	51
	13:41:59–14:13:22	Imaging	0.5	0.24	8191	1	31				51
	14:15:12–15:50:20	Imaging	0.2	0.20	65535	4	92				51
June 16	13:03:53–13:19:43	CW	–	0.20	–	–	14	53	+14	0.035	51
	13:23:52–13:47:39	Imaging	0.5	0.24	8191	1	21				51
	13:51:28–15:39:37	Imaging	0.2	0.20	65635	4	90				51
June 17	12:49:42–13:09:08	CW	–	0.40	–	–	15	51	+16	0.039	51
	13:13:24–15:28:37	Imaging	0.2	0.20	65535	4	102				51
June 18	12:34:48–13:00:37	CW	–	0.40	–	–	18	49	+18	0.044	51
	13:04:55–15:12:51	Imaging	1.0	0.40	8191	2	87				51
June 19	12:44:14–13:58:54	Imaging	1.0	0.40	8191	2	46	48	+20	0.048	51

Masterlog of 1994 CC radar observations. All observing dates refer to 2009. Observations were conducted monostatically with an average transmitter power of 60 kW at Arecibo and 430 kW at Goldstone. For the imaging data, the echoes were received in SC and OC polarizations at Arecibo but only in the OC polarization at Goldstone. Arecibo observations were at S-band (2380 MHz, 12.6 cm) and Goldstone observations were at X-band (8560 MHz, 3.5 cm). The times show the start and end of the reception of echoes for each setup on each day. The data resolution is given in time delay or baud ( $\mu\text{s}$ ) and Doppler frequency (Hz). “Code” refers to the length of the repeating binary phase code. The “ranging” data represent coarse imaging data that were used for the first-order orbital improvements. Some of Arecibo imaging data had multiple samples per baud (spb), allowing for finer time delay resolution. Right ascension, declination, and distance (in AU) are given at the beginning of each observation session. We also list the number of transmit–receive cycles (runs) and the orbital solution (Sol) used to compute delay-Doppler ephemeris predictions.

tional and data reduction techniques were nearly identical to those described in Magri et al. (2007).

The Doppler broadening (or bandwidth) of an echo is given by:

$$B = \frac{4\pi D}{\lambda P_r} \cos(\delta) \quad (1)$$

where  $B$  is the bandwidth,  $D$  is the object's maximum breadth in the plane of the sky perpendicular to the spin vector,  $\lambda$  is the radar wavelength (3.5 cm at Goldstone, 12.6 cm at Arecibo),  $P_r$  is the rotation period, and  $\delta$  is the subradar latitude.

Fig. 3A and B show continuous-wave (CW) echo power spectra obtained at Arecibo and Goldstone. For the Arecibo spectra, we

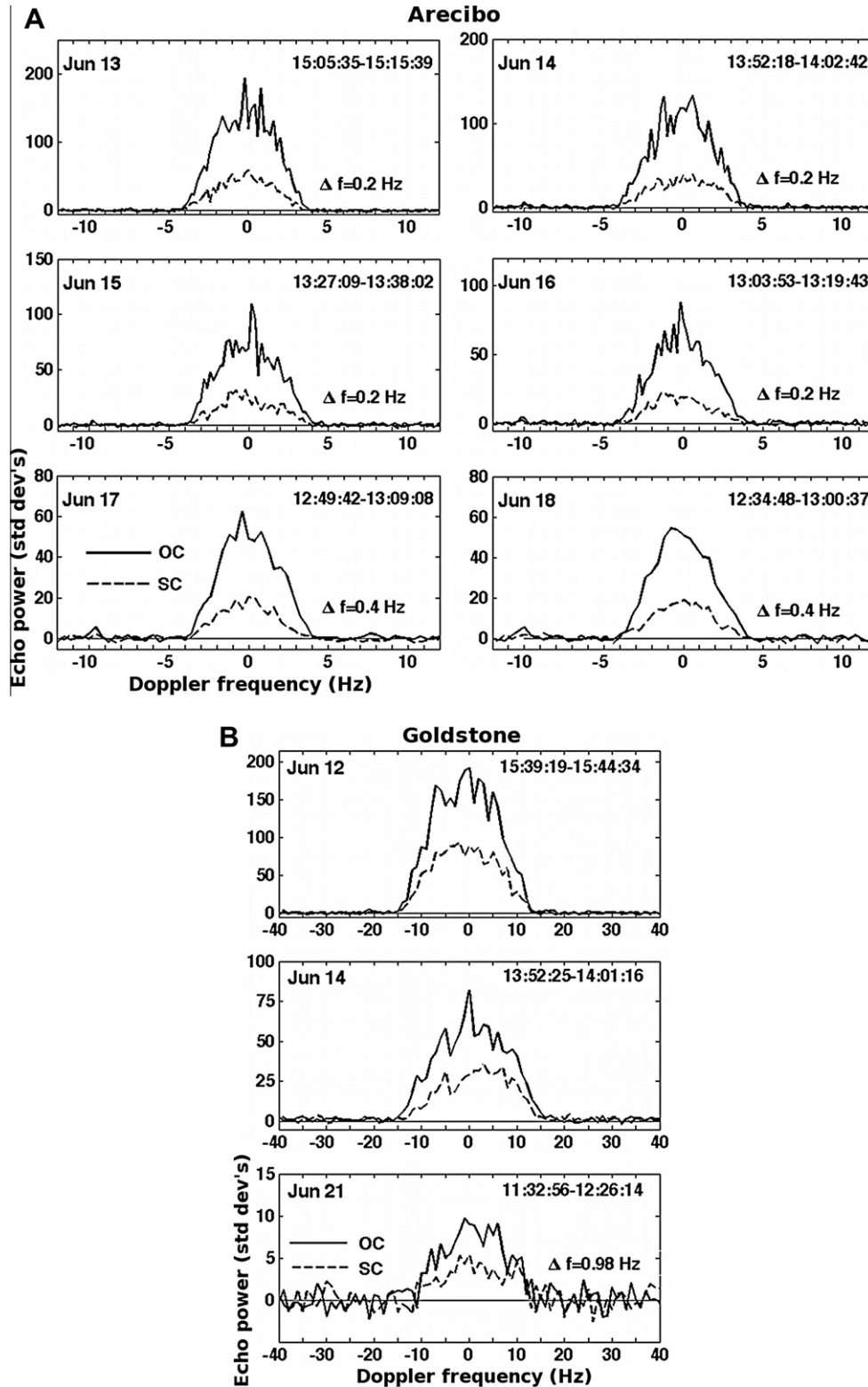


**Fig. 3.** (A) OC and SC echo power spectra for 1994 CC obtained at Arecibo. Each spectrum is a weighted sum of the number of runs from each day given in Table 2. In chronological order, the number of looks for each day is 39, 48, 44, 70, 195 and 252, respectively.  $\Delta f$  is the Doppler frequency resolution. (B) OC and SC spectra obtained at Goldstone. The number of looks is 117, 206, and 1313. Doppler frequency resolution is 0.98 Hz on all three dates.

measured the bandwidths between the innermost  $3\sigma$  crossing points (units of standard deviation of the off-echo noise); such bandwidth estimates are less affected by noise than if they were measured between the zero-crossing points. The bandwidths were all within 5% of 7.8 Hz. For the Goldstone data we measured bandwidths (also at  $3\sigma$ ) of  $28 \pm 1$  Hz on June 12,  $31 \pm 1$  Hz on June 14, and  $22 \pm 3$  Hz on June 21.

Fig. 4 shows Goldstone delay-Doppler images of the primary from June 12. Let us denote the primary as Alpha, the inner satellite as Beta, and the outer satellite as Gamma. The images cover slightly less than one full rotation of Alpha and are our best imaging data. Alpha appears to be a rounded and symmetric object. We measured the bandwidths and visible extents by counting contiguous pixels that are at least five standard deviations above the noise level. The bandwidth varies by  $<5\%$  as the object rotates, indicating low elongation, and the visible range extent also remains steady at about  $320 \pm 40$  m. If 1994 CC were a sphere, then we would see only half of the object, so for spherical objects, we estimate the true range extents by doubling the visible extents. This provides a zeroth-order estimate of the diameter. For 1994 CC, the estimated diameter is  $\sim 640$  m. If we combine this diameter with the mean of measured bandwidths ( $\sim 28$  Hz), then Eq. (1) gives rotation period of  $\sim 2.3 \text{ h} \times \cos(\delta)$ , which is consistent with the period estimated from the lightcurves if the subradar latitude is close to equatorial.

Alpha has few surface features at 19-m resolution. In some images in Fig. 4, the echo shows a cluster of pixels (marked as feature “A”) that gives the visual impression of the outline of a circular concavity that is located towards the center of the echo. There are also other, even more subtle radar-dark spots evident in several images. The appearance of the primary resembles that of 2008 EV5,

but without that object’s obvious concavity at the equator (Busch et al., 2011).

### 3. Satellites

Our initial Doppler resolution of 0.98 Hz on June 12 at Goldstone was too coarse to allow immediate detection of the satellites in the CW spectra. However, two satellites quickly became apparent in the real-time display of the delay-Doppler images (Fig. 5) that we obtained shortly after the CW data. We later checked the CW spectra with much finer resolution (0.2 Hz) but we did not see obvious echoes from either satellite. June 13 was the first day of observations at Arecibo and we used the highest available time-delay resolution ( $0.05 \mu\text{s}$  or 7.5 m). With this resolution Alpha and Beta were clearly visible but Gamma was not. Starting on June 14, we adopted a coarser  $0.2 \mu\text{s}$  (30 m) setup with 4 samples per baud, which still accomplishes an effective 7.5 m resolution while improving the SNRs (Magri et al., 2007). This setup revealed both satellites, which we detected until June 18. Gamma was observed one more time on June 19, although its echo strength was very weak.

We experimented with different Doppler resolutions and weighted sums of runs to study the echo bandwidths and sizes of the satellites. Goldstone can resolve the satellites better in Doppler frequency due to its higher transmitter frequency. However, Arecibo is more sensitive and it obtained images of the satellites at 2.5 times (7.5 m vs. 18.75 m) finer range resolution than Goldstone. In our attempt to resolve the satellites in both delay and Doppler frequency we had to balance the length of the data integration, which limits the Doppler resolution, while still

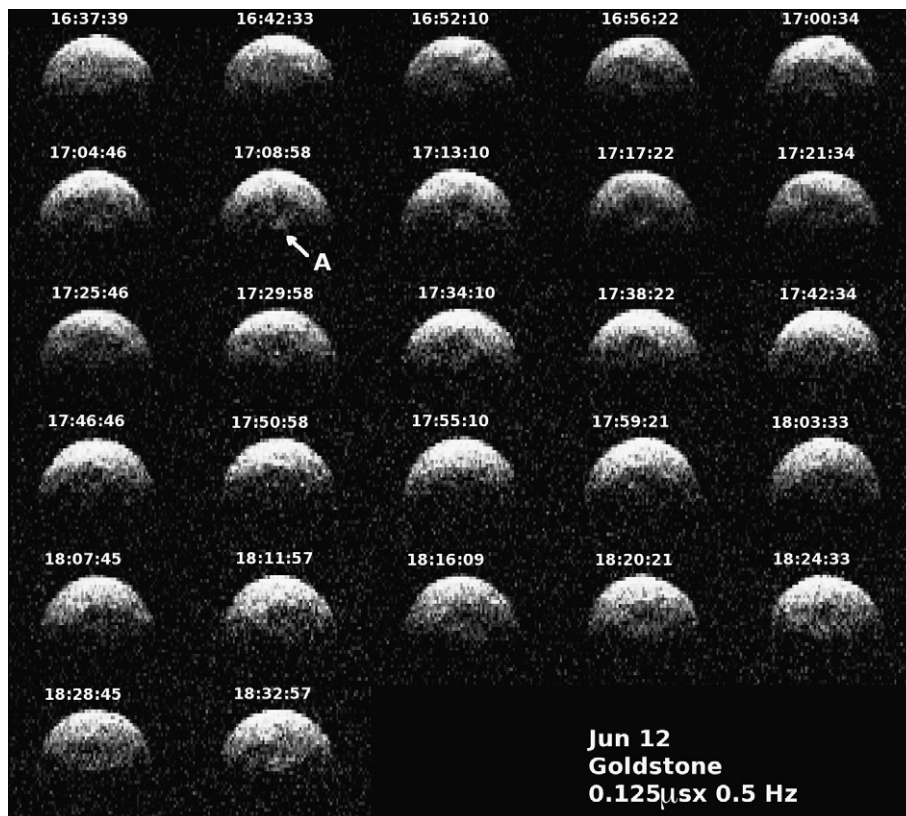
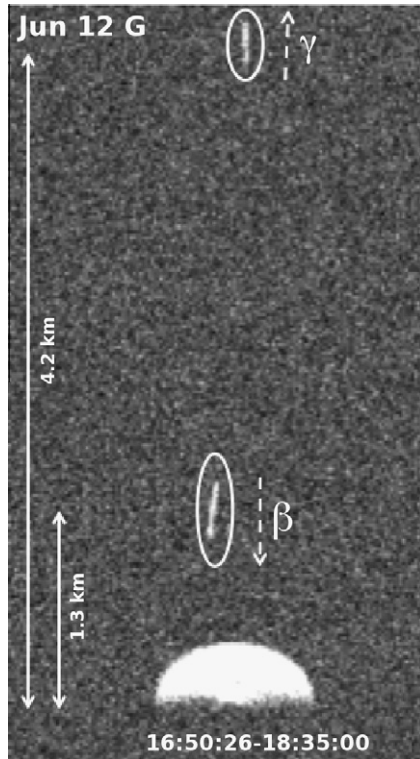


Fig. 4. Goldstone delay-Doppler images from June 12. The images are normalized so that the noise has zero mean and unit standard deviation. Each image covers  $\sim 11^\circ$  of rotation and is a sum of six runs. Times (UT) refer to the mid-epoch spanned by the data. Time delay increases from top to bottom and Doppler frequency increases from left to right, so rotation is counterclockwise. The resolution is  $0.125 \mu\text{s} \times 0.5$  Hz. The vertical dimension of each image is 1 km. “A” marks the radar bright feature that is discussed in the manuscript.



**Fig. 5.** Goldstone delay-Doppler image from June 12. This image is an integration spanning 1.74 h and covers  $263^\circ$  of rotation by Alpha. The contrast has been adjusted to show the satellites at the expense of saturating the echo from Alpha. Echoes from both satellites are smeared in range and Doppler frequency due to their orbital motion. Resolution is  $0.125 \mu\text{s} \times 0.50 \text{ Hz}$ . Both satellites are between Earth and Alpha. Solid lines on the left show the mean separations from Alpha; dashed white arrows indicate the direction of motion. Time delay and Doppler follow the same convention as described in Fig. 4.

maintaining the echo's strength. Short data integration intervals assure that the satellite's echo is not smeared in time delay, which could result in an overestimate of the satellite's size. At the same time, the echo must be strong enough to estimate the satellite's visible extent or we may underestimate the satellite's size. We estimate the visible extent and Doppler bandwidth for a satellite by counting the clustered pixels that are above a certain cut-off signal strength. For example, we processed  $0.05 \mu\text{s}$  Arecibo images from June 14 so that they have a very fine Doppler resolution of  $0.0156 \text{ Hz}$ . We summed 10 runs, collected during  $\sim 8.5 \text{ min}$  of physical time, to create a single delay-Doppler image. If we account for the transmit time and for the turret switching, this corresponds to only about  $\sim 3.3 \text{ min}$  of data integration time. Five consecutive

**Table 3**  
Satellite echo bandwidths, visible range extents, and estimated rotation periods.

Date	Obs	X-bandwidth (Hz)	S-bandwidth (Hz)	Visible range (m)	$P_r$ (h)
<i>Beta</i>					
June 12	G	$0.44 \pm 0.13$	$0.12 \pm 0.04$	$56.25 \pm 18.75$	$25.6 \pm 11.4$
June 14	A	$0.40 \pm 0.07$	$0.11 \pm 0.02$	$60.0 \pm 22.5$	$30.0 \pm 12.4$
June 15	A	$0.50 \pm 0.11$	$0.14 \pm 0.03$	$52.5 \pm 30.0$	$21.0 \pm 12.9$
<i>Gamma</i>					
June 12	G	$0.75 \pm 0.19$	$0.21 \pm 0.05$	$37.5 \pm 18.75$	$10.0 \pm 5.6$
June 14	A	$0.56 \pm 0.11$	$0.16 \pm 0.03$	$45.0 \pm 15.0$	$16.1 \pm 6.2$
June 15	A	$0.50 \pm 0.11$	$0.14 \pm 0.03$	$37.5 \pm 22.5$	$15.0 \pm 9.6$

Doppler bandwidths and visible range extents of Beta and Gamma estimated by visual inspection of delay-Doppler images with resolutions of  $18.75 \text{ m} \times 0.0628 \text{ Hz}$  at Goldstone (X-band) and  $7.5 \text{ m} \times 0.0156 \text{ Hz}$  at Arecibo (S-band). The uncertainties include our considerations of delay-Doppler imaging resolution, number of looks, as well as smearing of the echoes due to the satellites' motion. In order to facilitate direct bandwidth comparison, the bandwidths have been converted from S-band to X-band and vice versa. For a symmetric satellite, the total extent along the line of sight would be the double visible range extent. Rotational periods are calculated based on Eq. (1). Period uncertainties reflect the propagation of the bandwidth and the total extent (assumed diameter) errors.

delay-Doppler images are shown in Fig. 6. We considered a pixel to be part of the satellite if it has signal strength above  $1\sigma$  and it has neighboring pixels of equal or greater brightness, which is admittedly somewhat subjective. The leading edge of Beta moves by 3–4 pixels (22.5–30 m) between images whose mean times were separated by  $\sim 9 \text{ min}$ . This gave us a good estimate of the delay smearing within each image. Gamma moves more slowly than Beta and we estimated 2–3 pixels (15–22.5 m) of smearing in delay. Smearing in Doppler frequency due to the orbital motion is difficult to detect in our images and is at most 1 bin for both satellites, so we accounted for this in the bandwidth uncertainty.

Table 3 lists bandwidths and visible extents (with smearing subtracted) for Beta and Gamma estimated from delay-Doppler images obtained on June 12, 14 and 15; these are the only days when the SNRs were sufficient for size and bandwidth estimation. The uncertainties include our considerations of delay-Doppler imaging resolution and number of looks, as well as smearing of the echoes due to the satellites traveling along their orbits. The bandwidths suggest that both satellites could have moderate elongations. If we double the mean visible extent for each satellite from Table 3, then we obtain zeroth-order estimates of their diameters of  $113 \pm 30 \text{ m}$  for Beta and  $80 \pm 30 \text{ m}$  for Gamma. More precise estimates of their dimensions would require shape modeling, but the images do not have sufficient rotational coverage, SNRs, or resolution. We assign the diameter uncertainties based on the largest of the visible range uncertainties.

We used the mean bandwidths and estimated diameters from Table 3 in order to constrain the rotation periods of the satellites

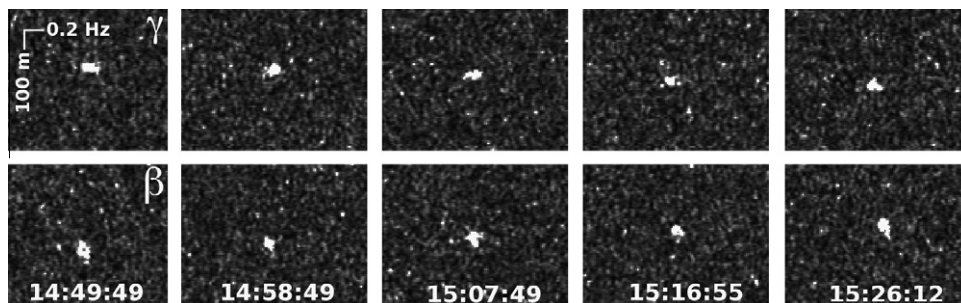


**Fig. 6.** Arecibo delay-Doppler images of Beta and Gamma on June 14. The images have a resolution of  $0.05 \mu\text{s} \times 0.0156 \text{ Hz}$  and each panel has a dimension of  $100 \text{ m} \times 0.2 \text{ Hz}$ . We summed 10 runs per image, with each run containing less than a half of a look due to fine Doppler resolution. The mid-epochs for the images are 9 min apart. Motion by Beta and Gamma is evident, as the coordinate centers of each image are held fixed.

via Eq. (1). If we assume that the subradar latitudes were close to equatorial, then this simplified approach suggests that Beta has a rotation period of  $26 \pm 12$  h and that Gamma has a period of  $14 \pm 7$  h. We adopted the rms of the mean in Table 3 as the uncertainty. This is also consistent with the errors on the individual period estimates.

In a companion paper, Fang et al. (2011) report orbital fits for Beta and Gamma that are based on the delay and Doppler separations listed in our Supplementary material. Briefly, they obtain semimajor axes of  $1.729 \pm 0.020$  km for Beta and  $6.130 \pm 0.108$  km for Gamma. Despite Gamma's large semimajor axis, it is still well within the Alpha's Hill sphere, which is  $\sim 86$  km in radius. The estimated orbital periods for Beta and Gamma are  $1.243 \pm 0.100$  days ( $29.832 \pm 2.400$  h) and  $8.376 \pm 0.500$  days ( $201.024 \pm 12.0$  h) respectively. Beta's orbital period is consistent with the rotational period estimated from the satellite's bandwidth, giving evidence for synchronous rotation, but Gamma's orbital period is much longer than its rotational period, thus indicating asynchronous rotation. Fang et al. (2011) also found that Beta's orbit is almost circular, while Gamma has an eccentricity of  $0.192^{+0.015}_{-0.022}$ . Beta's orbit was assumed to be in the equatorial plane of Alpha while Gamma appears to have  $\sim 16^\circ$  inclination.

#### 4. Shape modeling

We used the *Shape* software (Hudson, 1993 and Magri et al., 2007) to estimate Alpha's 3D shape and spin state. *Shape* utilizes a constrained, weighted least-squares minimization process and the input data may be delay-Doppler images, CW spectra, optical lightcurves, and/or plane-of-sky images. Our dataset contained weighted contributions from CW spectra and delay-Doppler images. Initially we did not use lightcurves in the shape modeling because they significantly slow down the fit, but we later added them after we obtained fits to the delay-Doppler images. The *Shape* modeling was guided by careful consideration of the initial parameters and penalty functions that assured uniform density, principal-axis rotation, and overall smooth appearance of the small-scale surface structure.

##### 4.1. Modeling dataset

The modeling dataset contains 19 Arecibo CW spectra and 161 delay-Doppler images from both Goldstone and Arecibo (summarized in the Supplementary material). The data cover eight consecutive days from June 12–19. The OC power spectra and delay-Doppler images were averaged in time to contain between  $11^\circ$  (June 12) and  $18^\circ$  (June 19) of rotation by Alpha. Our intention was to average as little rotation as possible while still maintaining good noise statistics and strong signal-to-noise ratios. As our observations progressed and the object grew more distant, we were forced to integrate data for longer periods of time at the expense of more rotational smearing.

The highest SNRs and best data came from Goldstone on June 12. This is the only day when some features are evident in the images. Later observations have weaker SNRs and they contribute to the final shape model primarily in terms of the bandwidth, visible extent, and shape of the leading edge. The four lightcurves (May 21, June 1–3) were included at the very end of the shape modeling, when the shape and pole direction were well constrained.

##### 4.2. Shape modeling of 1994 CC Alpha

In general, shape modeling consists of three stages. We start by approximating the shape of an asteroid with an ellipsoid. Our goal is to constrain the size, rotation period, and pole direction. Then we

use a more sophisticated model that parameterizes the shape with a set of a spherical harmonics. Finally, for a more accurate shape model, we parameterize the shape with a 3-D mesh made of triangular facets.

1994 CC Alpha is a very symmetric object with no pronounced features evident in the images, so an ellipsoid fit works very well. An ellipsoid is parameterized by three principal axis dimensions, all initially set at 0.6 km, as well as with three offsets in the  $x$ ,  $y$  and  $z$  directions from the center of mass, all initialized to zero.

We used a simple cosine law to model the radar scattering from the surface of the asteroid:

$$\frac{d\sigma}{dA} = R(C + 1)(\cos \alpha)^{2C} \quad (2)$$

Here,  $\sigma$  is the radar cross-section,  $A$  is the target surface area,  $\alpha$  is the scattering angle,  $R$  is the Fresnel reflectivity and  $C$  is a measure of the specularity of the scattering (Mitchell et al., 1996).

We conducted a grid search across the entire sky in order to constrain the pole direction. We searched ecliptic longitude,  $\lambda$ , from  $0^\circ$  to  $330^\circ$  in  $30^\circ$  increments and ecliptic latitude,  $\beta$ , in  $10^\circ$  increments from  $-85^\circ$  to  $+85^\circ$ . The ellipsoid fit eliminated  $\sim 40\%$  of the sky based on obvious bandwidth mismatches and poor  $\chi^2$  and left us with 126 candidate pole solutions. This selection is equivalent to keeping  $\lambda$  and  $\beta$  pairs that have subradar latitudes within  $30^\circ$  of the equator for the duration of our radar observations. Fig. 7 shows the results of the pole search; viable solutions appear as a broad white swath.

We explored each candidate pole with harmonic models. Given Alpha's symmetric shape, an eighth-order spherical harmonic series model is sufficient. We kept the spin state of each of 126 candidate poles fixed and we allowed the spherical harmonics coefficients to adjust in a way that minimizes  $\chi^2$ . The results were inconclusive regarding whether we can constrain the pole direction

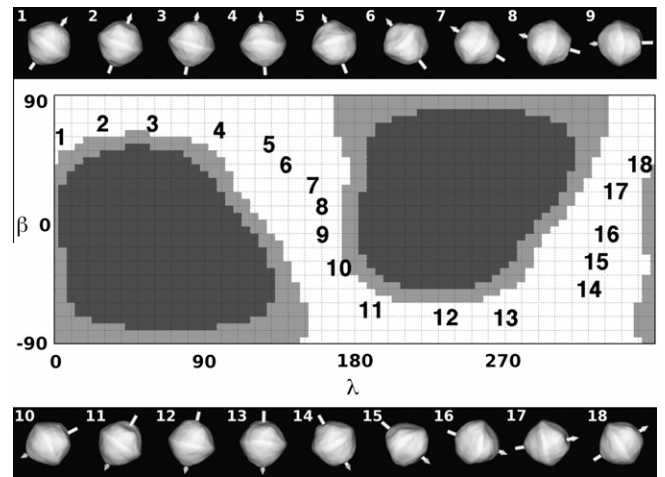


Fig. 7. Constraints on the pole direction of Alpha and shape models obtained from a suite of viable pole solutions. The middle panel shows the entire sky in ecliptic coordinates and the results of a grid search as a function of ecliptic longitude ( $\lambda$ ) and latitude ( $\beta$ ). Regions in white correspond to admissible pole solutions for Alpha in which the subradar latitude remains  $\leq 30^\circ$  from June 12 to June 19. The light gray regions show poles for which the subradar latitudes exceed  $30^\circ$  on at least one day, but remain  $\leq 40^\circ$  throughout the radar observations. Dark gray regions show subradar latitude larger than  $40^\circ$  that are incompatible with our radar data. Numbers in the middle panel show 18 pole solutions approximately evenly spaced in ecliptic longitude and latitude that give comparably good fits to the data. Panels at the top and bottom show plane-of-sky orientations of shape models corresponding to the 18 candidate pole directions indicated in the middle figure. The candidate poles coordinates are: 1 – ( $5^\circ, 60^\circ$ ); 2 – ( $30^\circ, 70^\circ$ ); 3 – ( $60^\circ, 70^\circ$ ); 4 – ( $100^\circ, 65^\circ$ ); 5 – ( $130^\circ, 55^\circ$ ); 6 – ( $140^\circ, 40^\circ$ ); 7 – ( $155^\circ, 25^\circ$ ); 8 – ( $160^\circ, 10^\circ$ ); 9 – ( $160^\circ, -10^\circ$ ); 10 – ( $170^\circ, -35^\circ$ ); 11 – ( $190^\circ, -65^\circ$ ); 12 – ( $235^\circ, -70^\circ$ ); 13 – ( $270^\circ, -70^\circ$ ); 14 – ( $320^\circ, -50^\circ$ ); 15 – ( $325^\circ, -30^\circ$ ); 16 – ( $330^\circ, -10^\circ$ ); 17 – ( $336^\circ, 22^\circ$ ); 18 – ( $350^\circ, 40^\circ$ ).

further; 117 out of 126 pole candidates were within 5% of the minimum  $\chi^2$  of 1.43. Although even a small difference in  $\chi^2$  may seem significant due to the large number of degrees of freedom ( $N = 1103838$ , given by the number of pixels in the delay-Doppler images and points in the CW spectra), visually, the models provided comparable matches to the data. All the models have an equatorial bulge, similar to those seen on the primaries of binary NEAs (66391) 1999 KW4 (Ostro et al., 2006) and 2004 DC (Taylor et al., 2008), and on non-binary 2008 EV5 (Busch et al., 2011). We found some pole solutions where the bulge is offset slightly from the equator, but despite such “muffin-top” shapes, the models match the observed bandwidths and delay extents well.

We parameterized the harmonic models with 2000 vertices that defined 3996 triangular facets. Magri et al. (2007) discuss in detail how we pick our modeling grid. In short, there is a trade-off between the resolution of our model (i.e. the object’s surface area divided by the number of vertices) and the computation time. However, our model’s final resolution is close to our data resolution. The vertex models spanned a suite of plausible pole solutions and Fig. 7 shows how the shape of Alpha changes as a function of  $\lambda$  and  $\beta$ . The models have a pronounced ridge that is sharp and localized on (or slightly off) the equator. The sizes of the principal axes are consistent among the models.

We explored the  $10^\circ \times 10^\circ$  region around the candidate pole for Alpha ( $\lambda = 334^\circ$ ,  $\beta = 18^\circ$ ) from our companion study by Fang et al. (2011) in  $5^\circ$  increments. In the final stages of the shape modeling, we allowed the poles to float. Our best  $\chi^2$  pole from that region is  $\lambda = 336^\circ$ ,  $\beta = 22^\circ$ , that is within  $5^\circ$  of the Fang et al. (2011) pole. This is model #17 in Fig. 7, which we adopted as our nominal model. This model has a symmetric appearance, an equatorial ridge at the center of the object, and it provides an excellent match to the large-scale features in our best delay-Doppler images. Table 4 summarizes the physical properties obtained by the shape modeling. Size variations among the different models are much smaller than the uncertainties listed in Table 4, but we felt that  $\sim 10\%$  uncertainties on the principal dimensions are appropriate in order to account for the data resolution and un-modeled sources of errors.

**Table 4**  
Physical properties of the 1994 CC Alpha model.

Pole direction ( $^\circ$ ): constrained to a white region in Fig. 7.			
Principal axes			
	X	$0.69^{+0.08}_{-0.04}$	km
	Y	$0.67^{+0.04}_{-0.08}$	km
	Z	$0.64^{+0.06}_{-0.06}$	km
Axis ratios			
	X/Y	$1.03 \pm 0.04$	
	Y/Z	$1.05 \pm 0.04$	
Equivalent diameter		$0.62 \pm 0.06$	km
Surface area		$1.25 \pm 0.20$	km <sup>2</sup>
Volume		$0.125 \pm 0.030$	km <sup>3</sup>
DEEVE			
	X	$0.63 \pm 0.06$	km
	Y	$0.62 \pm 0.06$	km
	Z	$0.61 \pm 0.06$	km
Rotation period		$2.3886 \pm 0.0001$ h	(from photometry)
Radar scattering law			
	R	$0.09 \pm 0.02$	
	C	$0.87 \pm 0.10$	
Optical albedo		$p_V = 0.42 \pm 0.10$	

Uncertainties in the physical dimensions and other properties were determined based on statistical variations between various modeling runs and by taking into account the imaging data resolution. “DEEVE” is the dynamically equivalent, equal volume ellipsoid. We also list the cosine radar scattering law parameters R and C (the value of parameter C roughly corresponds to Lambert scattering).

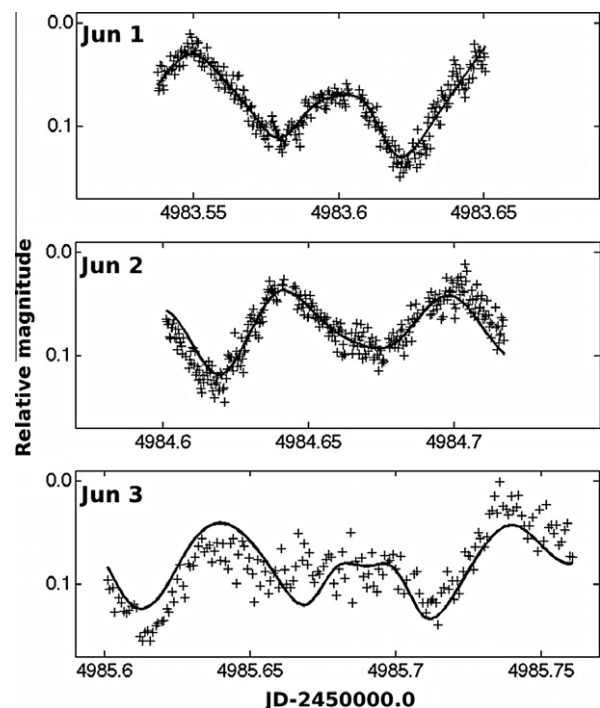
The orbital analysis by Fang et al. (2011) was based on delay-Doppler separations estimated from the shape modeling, so we revisited the lightcurves to test if the candidate mutual event in Fig. 1 is consistent with the nominal orbit for Beta. Fang et al.’s orbit for Beta predicts that the sub-radar latitude on June 3 at 00:58 UT was  $\sim 42^\circ$ , which would not allow for occultations or strong eclipses at that epoch. These conditions can occur between June 12 and 18, dates when lightcurves are unavailable.

We considered many other pole directions that could produce a mutual event on June 3 but we were unable to find a solution that simultaneously provides a good fit to the delay-Doppler images, to the delay-Doppler separations estimated from the images, and that also produces the candidate mutual event. Consequently, we do not consider the candidate mutual event in the June 3 lightcurves to be definitive.

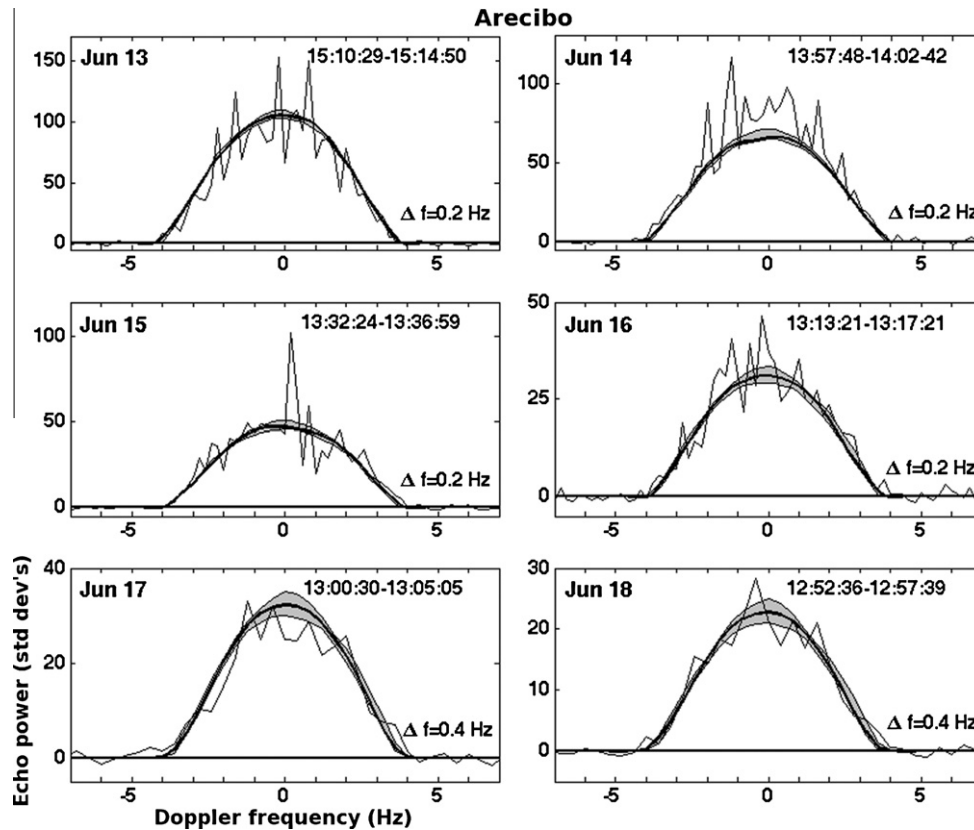
#### 4.3. Shape modeling fit to the data

Fig. 8 shows the lightcurve fits for the nominal pole ( $\lambda = 336^\circ$ ,  $\beta = 22^\circ$ ). We obtain comparable fits to the lightcurves with other the shape models as well. Fits to the May 21 lightcurve are not shown because those data contain such a significant amount of scatter that it is difficult to judge if the fit is meaningful. Our fits of the combined delay-Doppler images plus lightcurves were used to estimate the rotation period of Alpha and yielded  $P = 2.3886$  h that matches the value obtained earlier by fitting the lightcurves alone.

Fig. 9 shows selected OC echo power spectra used in the shape modeling and their respective fits (the rest are in the Supplementary material). The gray region marks the fit variations among all eighteen models shown in Fig. 7. Fits from our nominal model are marked with a thick black line. All the models match the bandwidths and provide decent fits to the spectral shapes. The majority of the CW  $\chi^2$  contributions come from the differences between the smooth, almost Gaussian fits and the jagged appearance of the data, which has been seen in fits to CW data for numerous other NEAs.



**Fig. 8.** Nominal shape model ( $\lambda = 336^\circ$ ,  $\beta = 22^\circ$ ) fit to the June 1–3 lightcurves. The candidate mutual event has been excluded from the June 3 lightcurve.



**Fig. 9.** Selected Arecibo OC echo power spectra obtained from June 13–18 and model fits. The fit from the nominal shape model ( $\lambda = 336^\circ$ ,  $\beta = 22^\circ$ ) is shown with a thick black line. The gray region shows the range of fits for all 18 shape models in Fig. 7.

Fig. 10 shows delay-Doppler data, fits, and plane-of-sky (POS) views obtained with the nominal model for June 12 and 14, when the SNRs were the strongest. The rest of the delay-Doppler data and their model fits are in the [Supplementary material](#). The nominal model successfully reproduces the bandwidths, visible extents, and the subtle surface structures such as the circular concavity at the center of the delay-Doppler echoes on June 12.

#### 4.4. 1994 CC Alpha's size and shape

Fig. 11 shows principal axis views of our nominal model. Alpha's shape has a prominent equatorial ridge and sloped hemispheres that closely resemble those on 1999 KW4 (Ostro et al., 2006), 2004 DC (Taylor et al., 2008), and 2008 EV5 (Busch et al., 2011). The feature labeled "A" in Fig. 4 appears to correspond to the flattened polar regions in the model. Flattened poles have also been noted on 2008 EV5 (Busch et al., 2011) and on the primary of 2004 DC (Taylor et al., 2008), another rapid rotator with a period of 2.57 h (R. Behrend, <http://obswww.unige.ch/~behrend/r04d00ca.png>). Because of the short rotation period and a nearly equatorial subradar latitude, our observations provided nearly complete surface coverage; there are only two small unconstrained patches around the poles where the incidence angle was greater than  $60^\circ$ . This is a conservative constraint on the incidence angle and we are inclined to believe that the slightly flattened polar region(s) are real. Most of the other candidate shape models in Fig. 7 also have at least one of their poles flattened, which suggest that this particular feature is required by the data.

Alpha's dimensions are  $X = 0.69^{+0.04}_{-0.08}$ ,  $Y = 0.67^{+0.04}_{-0.08}$ , and  $Z = 0.64^{+0.06}_{-0.06}$  km with an equivalent diameter of  $0.62 \pm 0.06$  km. Alpha is very symmetric and the ratio of X- and Y-axes is

$X/Y \approx 1.03 \pm 0.04$ , which indicates a low pole-on elongation. All uncertainties have been estimated based on the variations among the shape models in Fig. 7. Alpha's mass estimate of  $26 \pm 1 \times 10^{10}$  kg from Fang et al. (2011), and the volume of our model results in a density of  $2.1 \pm 0.6$  g cm $^{-3}$ . This is similar to the densities of 25143 Itokawa (Fujiwara et al., 2006), 1999 KW4 (Ostro et al., 2006), and 2000 DP107 (Margot et al., 2002a). The grain densities of meteorites that have been associated with S-class objects range from 3.7 g cm $^{-3}$  for ordinary chondrites (Consolmagno and Britt, 1998) to 5.1 g cm $^{-3}$  for stony irons (Wasson, 1974). Thus, 1994 CC Alpha's porosity is roughly between 41% and 57%, similar to that of 1999 KW4 Alpha's porosity (Ostro et al., 2006), and suggesting a rubble pile internal structure.

#### 4.5. Optical albedo

We estimate Alpha's visual geometric albedo based on the equivalent diameter from the shape modeling and its absolute visual magnitude of  $H_v = 17.6$ , which we obtained from JPL's Horizons on-line Solar System data and ephemeris computation service (Giorgini et al., 1996). The Horizon's assumed uncertainty on the absolute magnitude is  $\pm 0.3$ . We estimated the visual albedo using the expression  $p_v = (1329/D)^2 \times 10^{-0.4H_v}$  (Pravec and Harris, 2007) and obtained  $p_v = 0.42 \pm 0.10$ . The uncertainty was obtained by propagating errors in  $D$  and  $H_v$ . The albedo implies that 1994 CC Alpha is optically bright and it is consistent with the Sq taxonomy.

#### 5. 1994 CC orbit refinement

Radar astrometry data are referenced to the center-of-mass (COM) location of an asteroid's echo. During the observations,

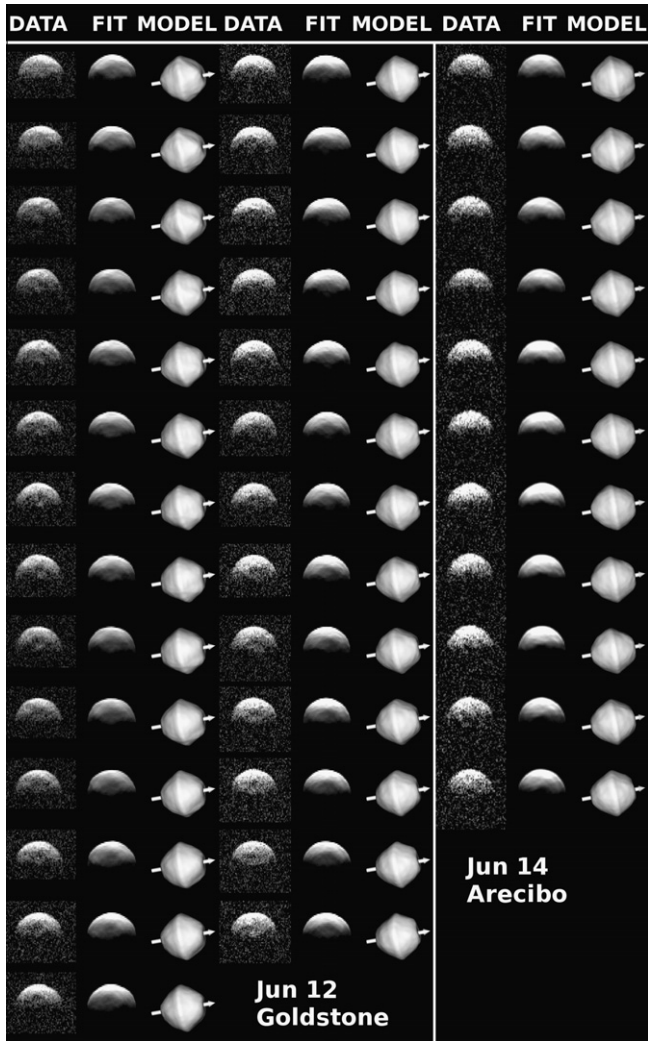


**Fig. 10.** Collage of, from left to right: delay-Doppler radar images, fits, and plane-of-sky renderings of the nominal shape model. In the data and fits, time delay increases from top to bottom, and Doppler frequency increases from left to right. The plane of sky view is contained in a  $1.0 \times 1.0$  km square with  $301 \times 301$  pixels. The white arrow shows the orientation of the spin vector.

the observer estimates this location and its uncertainty visually in time delay and Doppler frequency. One advantage of having a 3D model is that, with the assumption of homogeneous density, *Shape* gives precise locations of the center of mass and enables us to assign much smaller uncertainties than we previously estimated by eye, and thus significantly improves the orbit. The 14 Doppler and 13 time delay measurements estimated from the modeling appear in [Supplementary Table 4](#).

Fang et al. (2011) estimate that the mass ratios for the system are  $\text{Beta}/\text{Alpha} \approx 0.02$  and for  $\text{Gamma}/\text{Alpha} \approx 0.003$ . Their maximum influence on Alpha's center-of-mass, assuming that all three COMs occur on the same line and in Alpha's equatorial plane, is up to  $\sim 0.4 \mu\text{s}$  (60 m). Our data and assigned uncertainties are insensitive to this, although it is possible that the influence of the satellites on the Alpha's COM could be detected if a longer observing interval of  $0.05 \mu\text{s}$  delay-Doppler imaging were available.

We referenced our astrometry to the COMs obtained for the nominal model of Alpha, although the COMs of the other models are very similar and within the uncertainties that we assigned. We used the resulting astrometry to generate a new orbital fit (JPL orbital solution 84; see the [Supplementary material](#)).

The 2009 encounter with Earth was the closest over the entire interval over which the motion can be integrated reliably (see the online [Supplementary material](#)). Comparing solution #84 to an orbital solution that contains optical-only observations (380 measurements over 23 years), we find that the radar astrometry extends the interval of the predicted encounters by 40 years (4.3%). Encounter timing uncertainty is reduced by up to 23% at the limits of linearized prediction. This is in agreement with [Ostro and Giorgini \(2004\)](#) who concluded radar astrometry can improve the orbits even for objects with long optical arcs.

The next opportunity to observe 1994 CC with radar at SNRs comparable to those discussed here will occur in 2074. However, at Arecibo, we will be able to observe it at SNRs of a few hundred per day in 2032 and in 2053. 1994 CC will be a moderately good optical target in October of 2011. Photometric observations in the fall of 2011 could improve estimates of the pole direction, although this will be challenging due to the small lightcurve amplitude. Mutual events could be detected with 1.5–2 m-class telescopes.

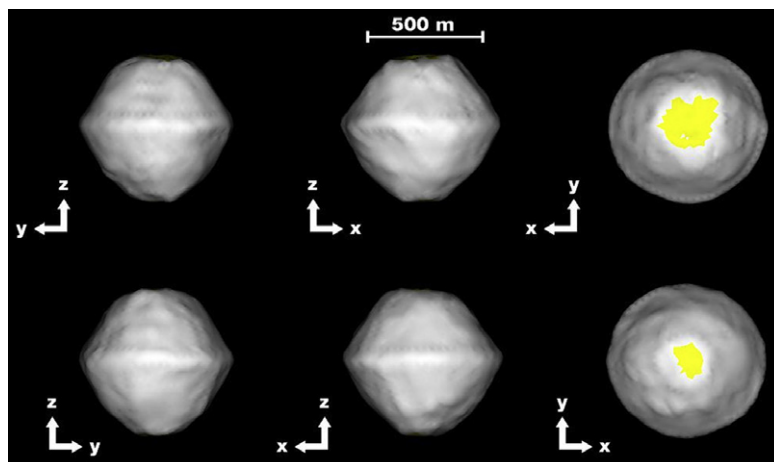


**Fig. 11.** Principal-axis views of the nominal 1994 CC Alpha shape model. The model is constructed from 2000 vertices that form 3996 triangular facets and have resolution of  $\sim (18 \text{ m})^2$ . Yellow shading indicates areas that are not well constrained by the data because the radar incidence angle was always greater than  $60^\circ$ . The model has dimensions of  $0.69 \times 0.67 \times 0.64$  km.

**Table 5**  
Disk-integrated properties.

Date	Time range (UTC) Start–Stop	Resolution (Hz)	Runs	Looks	$\sigma_{OC}$ (km <sup>2</sup> )	SC/OC	Area (km <sup>2</sup> )	$\eta_{OC}$
<i>Arecibo</i>								
June 13	15:05:35–15:09:56	0.2	6	18	0.035	0.40 ± 0.01	0.312	0.11
	15:10:29–15:14:50	0.2	6	18	0.037	0.41 ± 0.01	0.309	0.12
June 14	13:52:18–13:57:12	0.2	6	24	0.050	0.35 ± 0.01	0.311	0.16
	13:57:48–14:02:42	0.2	6	24	0.050	0.38 ± 0.01	0.311	0.16
June 15	13:27:09–13:31:44	0.2	5	20	0.047	0.36 ± 0.01	0.309	0.15
	13:32:24–13:36:59	0.2	5	20	0.043	0.40 ± 0.01	0.310	0.14
June 16	13:03:53–13:07:53	0.2	4	20	0.052	0.33 ± 0.01	0.304	0.17
	13:08:37–13:12:37	0.2	4	20	0.047	0.37 ± 0.01	0.304	0.16
	13:13:21–13:17:21	0.2	4	20	0.043	0.37 ± 0.02	0.304	0.14
	13:18:05–13:19:43	0.2	2	10	0.047	0.39 ± 0.01	0.308	0.15
June 17	12:49:42–12:54:17	0.4	4	52	0.036	0.46 ± 0.02	0.306	0.12
	12:55:06–12:49:41	0.4	4	52	0.039	0.42 ± 0.02	0.305	0.13
	13:00:30–13:05:05	0.4	4	52	0.028	0.33 ± 0.02	0.304	0.09
	13:05:54–13:09:08	0.4	3	39	0.040	0.36 ± 0.02	0.304	0.13
June 18	12:34:48–12:39:51	0.4	4	56	0.046	0.50 ± 0.03	0.309	0.15
	12:40:44–12:45:47	0.4	4	56	0.045	0.44 ± 0.02	0.307	0.15
	12:46:40–12:51:43	0.4	4	56	0.050	0.36 ± 0.02	0.306	0.16
	12:52:36–12:57:39	0.4	4	56	0.046	0.36 ± 0.02	0.304	0.15
	12:58:32–13:00:37	0.4	2	28	0.039	0.52 ± 0.03	0.304	0.13
					Average: 0.043 ± 0.011	0.40 ± 0.05		0.14 ± 0.04
<i>Goldstone</i>								
June 12	15:39:19–15:44:34	0.98	8	117	0.038	0.51 ± 0.01	0.303	0.13
June 14	13:52:25–14:01:16	0.98	10	206	0.034	0.50 ± 0.01	0.307	0.11
June 21	11:32:56–12:26:14	0.98	28	1313	0.028	0.49 ± 0.04	0.311	0.09
					Average: 0.033 ± 0.012	0.50 ± 0.02		0.11 ± 0.04

Disk-integrated OC cross section ( $\sigma_{OC}$ ) and circular polarization ratio (SC/OC) estimated from Arecibo and Goldstone CW spectra. Resolution in Doppler frequency was chosen in order to provide enough looks to obtain Gaussian noise statistics. The number of looks represents the number of statistically independent measurements that were used to get the average SC and OC spectra.

## 6. Disk-integrated properties

Table 5 lists disk-integrated properties for 1994 CC Alpha. Beta and Gamma make negligible contributions. The circular polarization ratios SC/OC are  $0.40 \pm 0.05$  and  $0.50 \pm 0.02$  for data obtained at Arecibo and Goldstone, respectively. The mean SC/OC for 214 near-Earth asteroids observed by radar is  $0.34 \pm 0.25$  (Benner et al., 2008a), suggesting the near-surface roughness of 1994 CC is slightly more rough than average. S-class NEAs have a mean SC/OC =  $0.27 \pm 0.08$  ( $N = 70$ ), indicating that 1994 CC is more rugged than most other Sq class NEAs detected by radar to date. The mean measured OC radar cross sections are  $\sigma_{OC} = 0.043 \pm 0.011$  km<sup>2</sup> for the Arecibo data and  $\sigma_{OC} = 0.033 \pm 0.012$  km<sup>2</sup> for the Goldstone data. Due to systematic calibration errors and many years of experience, we assigned uncertainties of 25% and 35% to radar cross sections estimated from data obtained at Arecibo and Goldstone, respectively. The OC radar albedo is calculated by dividing the measured OC cross section by the projected area of the model. We obtain radar albedos of  $\eta_{OC} = 0.14 \pm 0.04$  at Arecibo and  $\eta_{OC} = 0.11 \pm 0.04$  at Goldstone that are consistent within their uncertainties. These radar albedos are slightly lower than the average value reported,  $\eta_{OC} = 0.16 \pm 0.08$ ,  $N = 26$ , for other S-class NEAs ([http://echo.jpl.nasa.gov/~lance/asteroid\\_radar\\_properties/nea.radaralbedo.html](http://echo.jpl.nasa.gov/~lance/asteroid_radar_properties/nea.radaralbedo.html)).

## 7. 1994 CC's gravitational environment

The shape model for Alpha enables us to investigate its gravitational environment with an assumption of homogeneous density. The rapid rotation of the primary provides a strong constraint on the asteroidal slope, that is, the angle between the local acceleration vector and the outward surface normal. Densities below  $2.22$  g cm<sup>-3</sup> have gravitational slopes greater than  $90^\circ$  along the

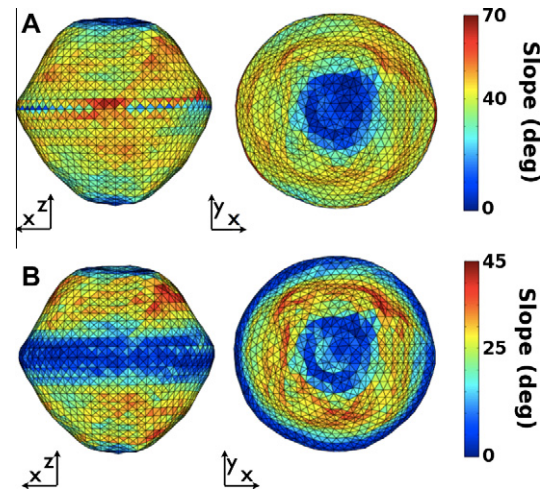


**Fig. 12.** Gravitational slopes for the nominal Alpha model. (A) Model density is  $2.25$  g cm<sup>-3</sup>. (B) Model density is  $3.0$  g cm<sup>-3</sup>. Note that the color scales in (A) and (B) are different.

equator, meaning that the surface has a net outward acceleration. Note that the density estimate based on the Fang et al. (2011) orbital fit and our Shape-based diameter is  $2.1 \pm 0.6$  g cm<sup>-3</sup> suggesting that Alpha's density is consistent with the threshold corresponding to net outward acceleration. Fig. 12A shows gravitational slopes for a density of  $2.25$  g cm<sup>-3</sup>. If we increase the density to  $3.0$  g cm<sup>-3</sup> (Fig. 12B), then the slopes become more subdued.

Fig. 13 shows the distribution of geopotential on the surface of Alpha assuming a density of  $2.25$  g cm<sup>-3</sup>. The geopotential is expressed in terms of the speed that a particle could obtain if it

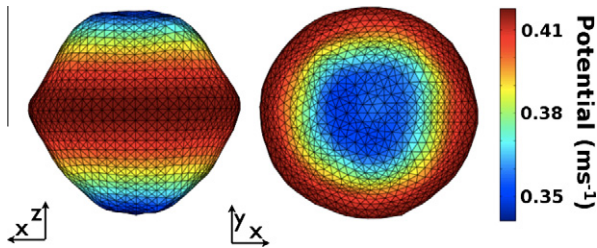


Fig. 13. Geopotential for the nominal Alpha model. Model density is  $2.25 \text{ g cm}^{-3}$ .

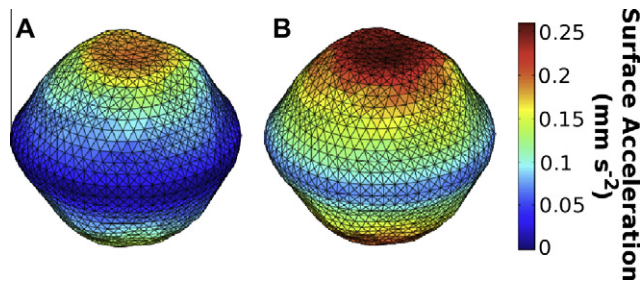


Fig. 14. Surface acceleration for the nominal Alpha model.  $1 \mu\text{G}$  is equal to  $0.01 \text{ mm s}^{-2}$ . (A) Model density is  $2.25 \text{ g cm}^{-3}$ . (B) Model density is  $3.0 \text{ g cm}^{-3}$ .

moves from a lower geopotential value to a higher geopotential value. Here, the larger speed means that the particle is deeper in the potential field, indicating that the minimum potential is along the equator. Fig. 13 shows that 1994 CC Alpha has a very similar potential distribution to that found for 1999 KW4 Alpha (Ostro et al., 2006), but is somewhat different from the one obtained for 2008 EV5 (Busch et al., 2011). 2008 EV5 rotates more slowly, leading to minimum potential energy being off the equator. Another way to state this is to say that for 1994 CC and 1999 KW4 the material is the least bound and thus easiest to reconfigure on the equator, whereas for 2008 EV5 this area occurs at mid-latitudes.

Fig. 14 shows the total acceleration normal to the surface for densities of  $2.25 \text{ g cm}^{-3}$  and  $3.0 \text{ g cm}^{-3}$ . This shows that the equatorial acceleration is near zero for the lower density, but is definitely non-zero for the larger density.

## 8. Discussion

### 8.1. Abundance of multiple systems in the NEA population

Radar and photometric observations suggest that about 16% of NEAs larger than  $\sim 200 \text{ m}$  in diameter are binary systems (Margot et al., 2002a; Pravec et al., 2006). Since completion of the upgrade at Arecibo in 1999, 26 binaries and 2 triples have been observed by radar out of 173 asteroids  $\geq 200 \text{ m}$  in diameter. In addition, there are eight confirmed binaries that have not yet been observed by radar. 1994 CC is only the second confirmed triple system after 2001 SN263. Other than these two confirmed cases, there is one unconfirmed candidate, 2002 CE26, that showed the possible signature of a second satellite in Arecibo images on a single day (Shepard et al., 2006). Taken at face value, and if the objects imaged by radar are representative, then radar observations hint that a few percent of multiple NEAs and perhaps  $\sim 1\%$  of NEAs larger than  $\sim 200 \text{ m}$  in diameter are triple systems.

Table 6 lists known binaries/triple systems, the sizes of the components, as well as their separations,  $S$ , estimated from radar and/or optical data. The diameters of the primaries range from  $0.12 \text{ km}$  for 2003 SS84 to  $\sim 9 \text{ km}$  for Sisyphus. The diameters of the satellites range from  $0.05 \text{ km}$  for 2000 CO101 to  $\sim 1 \text{ km}$  diam-

eter for 2001 SN263 Beta. Binaries (185851) 2000 DP107, (66391) 1999 KW4, (276094) 2002 CE26, 2004 DC, and both triples have reasonably well-determined satellite orbits. For those objects, the average separations correspond to their semimajor axes. For other objects observed by radar for which the orbital elements are not known, we list the maximum separation that we observe in the radar data. The semimajor axis may be smaller, equal to, or larger than the maximum observed separation. We also list the semimajor axes estimated obtained from lightcurves (Pravec and Harris, 2007). As pointed out by Pravec et al. (2006), most systems have satellites relatively close to the primary with normalized separations (defined as  $S/(R1 + R2)$ , where  $R1$  and  $R2$  are the radii of the primary and the secondary) less than 5.

Table 6 has interesting implications for the abundance of crater pairs on Earth due to the impacts of binary systems. Bottke and Melosh (1996a,b) found that  $3/28$  ( $\sim 10\%$ ) of the largest terrestrial impact craters occur in closely-spaced crater pairs, which they interpreted as evidence for collisions by binary asteroids. Bottke and Melosh modeled binary asteroid formation via tidal stripping of rapidly rotating contact binaries during close terrestrial planet flybys and estimated that binaries comprise  $\sim 15\%$  of the NEA population. The Bottke and Melosh papers appeared shortly before 1994 AW1, the first candidate binary NEA, was reported in the peer-reviewed literature by Pravec and Hahn (1997). Subsequently, confirmation that NEAs have satellites came from Goldstone and Arecibo radar observations that spatially resolved 2000 DP107 into two objects and revealed their mutual motion (Margot et al., 2002a). Margot et al. (2002a) and Pravec et al. (2006) found that  $\sim 16\%$  of NEAs larger than  $\sim 200 \text{ m}$  in diameter are binary systems, an abundance that appears consistent with the prediction published by Bottke and Melosh (1996a,b).

Terrestrial crater separations scaled to the sum of the components' radii are 7.5 for the Kamensk-Gusev craters in Russia, 11 for East and West Clearwater Lakes in Canada, and 35 for Reiss-Steinheim craters in Germany (Bottke and Melosh, 1996a,b). Table 6 shows that among the 36 binary and triple systems observed with radar and/or photometry, only three, 1998 ST27, 2001 SN263, and 1994 CC, have at least one companion with a separation comparable to, or exceeding, the closest separation observed among terrestrial crater pairs. Thus,  $3/173$  ( $\sim 2\%$ ) of NEAs with diameters equal-or-greater than  $200 \text{ m}$  observed by radar since 1999 have satellites with sufficient separations to produce pairs of craters. This is a much lower percentage than suggested by Bottke and Melosh (1996a,b) whose tidal disruption model produced binaries with large separations between their components. Terrestrial crater diameters are typically  $\sim 10$ – $20$  times larger than their progenitors and most of the known binary NEAs are so closely spaced that they would produce only a single crater if they were to impact Earth.

More recently, the origin of binaries has been explained with the non-gravitational YORP (Yarkovsky–O'Keefe–Radzievskii–Paddack) effect (Scheeres, 2007; Walsh et al., 2008; Jacobson and Scheeres, 2011). Briefly, when incident sunlight is thermally re-radiated from the surface of an irregularly-shaped, rotating asteroid, it provides a small but continuous torque. The YORP effect can accelerate the rotation to the point of rotational disruption, thus creating a satellite. Walsh et al. (2008) used numerical simulations to study how YORP creates binaries. They modeled the primary as a rubble pile that is spun up by the thermal re-radiation to the point that it starts to shed the mass from the equator, thus forming a satellite. This model produced closely-spaced binaries whose separations and rotation periods closely resemble those of the observed systems. More recently, Jacobson and Scheeres (2011) showed that YORP induced fission of rubble pile asteroids, as opposed to gradual equatorial mass shedding, can produce contact binary, binary, and ternary systems with a wide variety of physical and orbital

**Table 6**  
 Sizes and separations of near-Earth binaries and triples.

Binary system	D1 (km)	D2 (km)	S (km)	S/(R1 + R2)	References
1998 ST27	0.80	0.12	~7.0	~15.2	Benner et al. (2003)
(164121) 2003 YT1	1.10	0.21	~2.7	~4.1	Nolan et al. (2004)
	(1.00)	(0.18)	(3.2)	(5.4)	Pravec and Harris (2007)
(185851) 2000 DP107	0.80	0.30	2.6	4.7	Margot et al., (2002a)
			(2.9)	(5.1)	Pravec and Harris (2007)
(35107) 1991 VH	1.20	0.45			Margot et al. (in prep)
	(1.20)	(0.45)	(3.6)	(4.4)	Pravec and Harris (2007)
					Pravec et al. (1998)
(3671) Dionysus	1.50	0.30	(4.0)	(4.4)	Pravec and Harris (2007)
					Mottola et al. (1997)
(162000) 1990 OS	0.30	0.05	~0.6	~3.4	Ostro et al. (unpublished)
			(0.7)	(4.0)	Pravec and Harris (2007)
					Ostro et al. (2003)
2008 BT18	0.60	0.20	~1.5	~3.8	Benner et al. (unpublished)
					Benner et al. (2008b)
2004 DC	0.36	0.07	~0.8	~3.7	Taylor et al. (2008)
(1862) Apollo	1.60	0.08	~3.0	~3.6	Ostro et al. (2002, 2005)
2002 BM26	0.60	0.10	~1.2	~3.4	Nolan et al. (unpublished)
					Nolan et al. (2002a)
2005 AB	1.90	0.46	(3.8)	(3.2)	Reddy et al. (2006a)
					Pravec and Harris (2007)
1994 AW1	1.00	0.48	(2.4)	(3.2)	Pravec and Harris (2007)
(7088) Ishtar	1.20	0.50	(2.7)	(3.2)	Pravec and Harris (2007)
					Reddy et al. (2006b)
(66391) 1999 KW4	1.32	0.45	2.6	2.9	Ostro et al. (2006)
(175706) 1996 FG3	1.84	0.46	(2.8)	(2.9)	Mueller et al. (2011)
					Pravec and Harris (2007)
(88710) 2001 SL9	0.80	0.22	(1.5)	(2.9)	Pravec and Harris (2007)
(137170) 1999 HF1	3.50	0.80	(6.0)	(2.8)	Pravec and Harris (2007)
(85938) 1999 DJ4	0.35	0.20	~0.7	~2.5	Benner et al. (unpublished)
	(0.35)	(0.17)	(0.7)	(2.7)	Pravec and Harris (2007)
(65803) Didymos	0.80	0.15	~1.2	~2.5	Benner et al. (2010)
	(0.75)	(0.17)	(1.1)	(2.5)	Pravec and Harris (2007)
2002 CE26	3.50	0.30	4.7	2.5	Shepard et al. (2006)
(31345) 1998 PG	0.90	0.34	(1.5)	(2.4)	Pravec and Harris (2007)
(5381) Sekhmet	1.00	0.30	~1.5	~2.3	Neish et al. (2004)
2006 VV2	1.80	0.50	~2.4	~2.1	Benner et al. (2007a)
2006 GY2	0.40	0.08	~0.5	~2.1	Benner et al. (unpublished)
			(0.60)	(2.5)	Pravec and Harris (2007)
					Benner et al. (2006)
2000 CO101	0.53	0.05	~0.6	~2.1	Taylor et al. (unpublished)
					Taylor et al. (2009)
2007 DT103	0.30	0.08	~0.4	~2.1	Benner et al. (unpublished)
			(0.55)	(2.9)	Pravec and Harris (2007)
					Benner et al. (2007b)
2000 UG11	0.23	0.09	0.43	~1.9	Nolan et al. (2000)
	(0.26)	(0.15)	(0.56)	(2.7)	Pravec and Harris (2007)
					Margot et al. (2002b)
2005 NB7	0.50	0.20	~0.6	~1.7	Shepard et al. (unpublished)
			(0.9)	(2.6)	Pravec and Harris (2007)
					Kušnirák et al. (2008)
					Shepard et al. (2008)
(69230) Hermes	~0.6	~0.54	~0.6	~1.1	Margot et al. (unpublished)
			(1.2)	(2.1)	Pravec and Harris (2007)
					Margot et al. (2003)
(66063) 1998 RO1	0.80	0.60	~0.8	~1.1	Benner et al. (unpublished)
	(0.80)	(0.38)	(1.4)	(2.4)	Pravec and Harris (2007)
2003 SS84	0.12	0.06	~0.1	~1.1	Nolan et al. (unpublished)
					Nolan et al. (2003)
1994 XD	0.60	0.15	~0.3	~0.8	Benner et al. (unpublished)
					Benner et al. (2005)
2002 KK8	0.50	0.10	~0.2	~0.7	Nolan et al. (unpublished)
					Nolan et al. (2002b)
(1866) Sisyphus <sup>a</sup>	~9.00	–	–	–	Ostro et al. (unpublished)
	(8.20–13.20)				Veeder et al. (1989)

(continued on next page)

**Table 6** (continued)

	$D1$ (km)	$D2$ (km)	$D3$ (km)	$S12$ (km)	$S13$ (km)	Radar references
Triple system (136617) 1994 CC	0.62	0.11	0.08	1.7	6.1	This paper Fang et al. (2011)
(153591) 2001 SN263	2.60	0.40	1.00	3.8	16.6	Nolan et al. (2008) Fang et al. (2011)
	$S12/(R1 + R2)$		$S13/(R1 + R3)$			Radar references
Triple system (136617) 1994 CC	4.7		17.5			This paper Fang et al. (2011)
(153591) 2001 SN263	2.5		9.2			Nolan et al. (2008) Fang et al. (2011)

Binary and triple systems ranked by the descending order of their separation ratio,  $S/(R1 + R2)$ , where  $S$  is the maximum observed separation between the primary and the satellite in the radar data or the satellite's semimajor axis estimate,  $R1$  and  $R2$  are the radii of the primary and satellite. The table also lists diameters,  $D1$  and  $D2$ , for each component. Quantities in parentheses were estimated from lightcurve data (Pravec and Harris, 2007). An updated version of the orbital data from Pravec and Harris (2007) can be found at <http://www.asu.cas.cz/~asteroid/binastdata.htm>.

<sup>a</sup> Steve Ostro observed Sisyphus on four dates in December of 1985 at Arecibo. CW spectra revealed a narrowband feature or “spike” that moved from day-to-day. This feature is most likely a satellite.

properties; this work has potentially profound implications for the origins of these bodies. Satellite orbits can also evolve by tidal forces between the bodies (Taylor and Margot, 2010), solar gravitational perturbations, and possibly the binary YORP (BYORP) effect (Čuk and Burns, 2005; Goldreich and Sari, 2009). BYORP theory describes orbital changes that occur due to the thermal torque that is a result of a re-radiation imbalance from the leading and trailing hemispheres of a synchronous satellite. BYORP has yet to be confirmed with direct observations (McMahon and Scheeres, 2010).

Why are there more pairs of terrestrial impact craters than binary or triple systems with sufficient separations to produce them? Although we cannot say with certainty, there are several plausible explanations. First, only three crater pairs and three widely-separated satellite systems have been discovered, so this is in the realm of small number statistics and comparisons may not be meaningful. Second, the ages of the crater pairs range from a minimum of  $14.8 \pm 0.7$  Ma for the Ries-Steinheim craters (Grieve, 1987) in Germany to a maximum of  $290 \pm 20$  Ma for East and West Clearwater Lakes in Canada (Grieve, 1987). Perhaps the NEA population has changed. There are also geologic selection effects that could skew the cratering record; for example, the Clearwater Lakes craters are on the Canadian Shield, which has not been tectonically deformed for hundreds of millions of years, and is thus more likely to preserve craters than a younger, more active geologic unit. There are also biases that affect our ability to detect distant companions in delay-Doppler radar data, most notably the signal-to-noise ratios, which are a strong function of the object's distance from Earth. All three of the most distant companions were relatively weak radar targets that were not well resolved in the radar images. Radar SNRs are proportional to  $P_r^{1/2}$  and  $D^{3/2}$ , where  $P_r$  is the rotation period and  $D$  is the diameter, so small, rapid rotators are more difficult

to detect than larger, slowly-rotating satellites in synchronous orbits about their primaries. Furthermore, if the Doppler resolution in the images is much finer or much coarser than the satellite's bandwidth, then a satellite's echo will have a low apparent SNR and could escape notice. Finally, many asteroids that made close approaches were not observed with radar due to scheduling conflicts, equipment problems, and/or insufficient advance notice.

## 8.2. Asynchronously rotating satellites

Table 7 lists binary and triple systems with asynchronously rotating satellites: at least 7 out of 28 (25%) of the multiple systems observed by radar have a satellite whose rotation ( $P_r$ ) and orbital ( $P_o$ ) periods differ substantially. This is a lower limit because estimates of the orbital and rotational periods are available for only 57% (16/28) of the multiple systems observed by radar. All seven asynchronous satellites rotate more rapidly than their orbital periods. The implication is that a significant fraction of NEA satellites are not tidally locked and that rotation periods more rapid than orbital periods are relatively common among satellites of binary and ternary NEAs.

According to BYORP theory, if a satellite rotates asynchronously, then the radiative forces and the net torque that produces a secular acceleration average out to zero and the orbital evolution due to BYORP shuts down. This could have some important consequences for the longevity of a multiple system. BYORP is thought to act quickly ( $\sim 10^5$  years, Čuk (2007)), and result in a satellite merger with the primary or tidal stripping of the satellite from the system (Čuk and Nesvorný, 2010). McMahon and Scheeres (2010) found that BYORP can expand the orbits to the Hill radius of the primary within  $10^4$ – $10^6$  years. McMahon and Scheeres (2010) argued that

**Table 7**  
Asynchronous NEA satellites.

	$P_o$	$P_r$	References
<i>Binary system</i>			
1998 ST27	>7 days	≤6 h	Benner et al. (2003)
(164121) 2003 YT1	~30 h	≤6 h	Nolan et al. (2004)
(35107) 1991 VH	~33 h	~13 h	Pravec et al. (2006)
(162000) 1990 OS	~21 h	≤8 h	Ostro et al. (unpublished)
2004 DC	~23 h	≤6.5 h	Taylor et al. (2008)
<i>Triple system</i>			
(136617) 1994 CC	~8.4 days	~14 h	This paper; Fang et al. (2011)
(153591) 2001 SN263	~6.2 days	~13 h	Nolan et al. (2008), Fang et al. (2011)

Orbital ( $P_o$ ) and rotational ( $P_r$ ) periods for the asynchronous NEA satellites. Note that all the satellites rotate more rapidly than their orbital periods.  $P_r$  is estimated based on the radar data and we assume near-equatorial orientation of the satellite.

orbital evolution due to BYORP is too fast to explain the relative abundance of binaries in the NEA population. They suggested that a rapidly spinning primary either goes through the multiple cycles of becoming a binary during its nominal lifetime of  $\sim 10^7$  years (Gladman et al., 2000) or the orbital changes due to BYORP get shut down or delayed via loss of synchronous rotation. Given the high percentage of asynchronous satellites in our radar sample, we suspect that a loss of synchronous rotation plays an important role in the lifespan of a multiple system.

How do orbits of the satellites become asynchronous? Čuk and Nesvorný (2010) showed that BYORP-driven outward orbital migration of a synchronous satellite can be stopped by the onset of chaotic rotation or a higher-order spin-orbit resonance. The satellite can again enter synchronous rotation if the orbit shrinks and circularizes. Jacobson and Scheeres (2011) found that some binaries acquire large eccentricities “at birth” that never damp to circular orbits. Thus, the secondary never synchronizes. They have also found that “birth” of another satellite by fission from a rapidly spinning secondary may destabilize the rotation of the original piece. The outer satellites for both 1994 CC and 2001 SN263 systems are asynchronous. Were they the original parent-body for the inner satellites? Their rotation periods of  $\sim 14$  and  $\sim 13$  h respectively, are slow compared to the rotation rates that are necessary for disruption of an asteroid of their respective sizes (Pravec and Harris, 2000). In fact, none of the satellites’ rotational periods, synchronous or asynchronous (Table 8 in Pravec and Harris, 2007), are spinning at rates that would make the fission plausible. The absence of satellite rotation periods  $< 3$  h in Table 8 in Pravec and Harris (2007) is intriguing, although the statistics on the rotational periods of satellites is still low and several rotation periods are only the upper bounds.

The discovery of triple systems in the NEA population generates even more questions than were raised initially with the discovery of binaries. Could there be more than two satellites in orbit around a near-Earth asteroid? What is a lifetime of a triple system? Did the satellites form when the asteroid was still in the Main Belt? Further radar and optical observations of more multiple NEAs may suggest answers to these questions.

## Acknowledgments

We thank Kevin Walsh and Darin Ragozzine for their insightful reviews, which improved our manuscript. We thank the Arecibo and Goldstone technical and support staffs for help with the radar observations. The Arecibo Observatory is part of the National Astronomy and Ionosphere Center (NAIC), which is operated by Cornell University under a cooperative agreement with the National Science Foundation (NSF). The work at Ondřejov has been supported by the Grant Agency of the Czech Republic, Grant 205/09/1107. The work at Modra has been supported by the Slovak Grant Agency for Science VEGA, Grant 2/0016/09. Some of this work was performed at the Jet Propulsion Laboratory, California Institute of Technology, under contract with National Aeronautics and Space Administration (NASA). This material is based in part upon work supported by NASA under the Science Mission Directorate Research and Analysis Programs.

## Appendix A. Supplementary material

Supplementary data associated with this article can be found, in the online version, at doi:10.1016/j.icarus.2011.09.002.

## References

Benner, L.A.M., Nolan, M.C., Margot, J.L., Ostro, S.J., Giorgini, J.D., 2003. Radar imaging of binary near-Earth Asteroid 1998 ST27. *Bull. Am. Astron. Soc.* 35, 959.

- Benner, L.A.M., Nolan, M.C., Ostro, S.J., Giorgini, J.D., Margot, J.L., Magri, C., 2005. 1994 XD. *IAU Circ.* 8563.
- Benner, L.A.M., Nolan, M.C., Shepard, M.K., Giorgini, J.D., Ostro, S.J., Busch, M.W., Hine, A.A., 2006. 2006 GV2. *CBET* 534.
- Benner, L.A.M. et al., 2007a. Radar images of binary near-Earth Asteroid 2006 VV2. *Bull. Am. Astron. Soc.* 39, 432.
- Benner, L.A.M. et al., 2007b. 2007 DT103. *IAU Circ.* 8866.
- Benner, L.A.M. et al., 2008a. Near-Earth asteroid surface roughness depends on compositional class. *Icarus* 198, 294–304.
- Benner, L.A.M. et al., 2008b. 2008 BT18. *CBET* 1450.
- Benner, L.A.M. et al., 2010. Radar imaging and a physical model of binary Asteroid 65803 Didymos. *Bull. Am. Astron. Soc.* 42, 1056.
- Binzel, R.P., Rivkin, A.S., Thomas, C.A., Vernazza, P., Burbine, T.H., DeMeo, F.E., Bus, S.J., Tokunaga, A.T., Birlan, M., 2009. Spectral properties and composition of potentially hazardous Asteroid (99942) Apophis. *Icarus* 200, 480–485.
- Bottke Jr., W.F., Melosh, H.J., 1996a. Binary asteroids and the formation of doublet craters. *Icarus* 124, 327–391.
- Bottke Jr., W.F., Melosh, H.J., 1996b. Formation of asteroid satellites and doublet craters. *Nature* 381, 51–53.
- Bus, S.J., Binzel, R.P., 2002. Phase II of the small main-belt asteroid spectroscopic survey: A feature-based taxonomy. *Icarus* 158, 146–177.
- Busch, M.W. et al., 2011. Radar observations and the shape of near-Earth Asteroid 2008 EV5. *Icarus* 212, 649–660.
- Consolmagno, G.J., Britt, D.T., 1998. The density and porosity of meteorites from the Vatican collection. *Meteor. Planet. Sci.* 33, 1231–1241.
- Čuk, M., 2007. Formation and destruction of small binary asteroids. *Astrophys. J.* 659, L57–L60.
- Čuk, M., Burns, J.A., 2005. Effects of thermal radiation on the dynamics of binary NEAs. *Icarus* 176, 418–431.
- Čuk, M., Nesvorný, D., 2010. Orbit evolution of small binary asteroids. *Icarus* 207, 732–743.
- Fang, J., Margot, J.-L., Brozovic, M., Nolan, M.C., Benner, L.A.M., Taylor, P.A., 2011. Orbits of near-Earth asteroid triples 2001 SN263 and 1994 CC: Properties, origin, and evolution. *Astron. J.* 141, 154–168.
- Fujiwara, M. et al., 2006. The rubble-pile asteroid Itokawa as observed by Hayabusa. *Science* 312, 1330–1334.
- Giorgini, J.D. et al., 1996. JPL’s on-line Solar System data service. *Bull. Am. Astron. Soc.* 28, 1158.
- Gladman, B., Michel, P., Froeschlé, C., 2000. The near-Earth object population. *Icarus* 146, 176–189.
- Goldreich, P., Sari, R., 2009. Tidal evolution of rubble piles. *Astrophys. J.* 691, 54–60.
- Grieve, R.A.F., 1987. Terrestrial impact structures. *Ann. Rev. Earth Planet. Sci.* 15, 245–270.
- Harris, A.W., Lupishko, D.F., 1989. Photometric lightcurve observations and reduction techniques. In: Binzel, R.P., Gehrels, T., Matthews, M.S. (Eds.), *Asteroids II*. University of Arizona Press, Tucson, pp. 39–53.
- Harris, A.W. et al., 1989. Photoelectric observations of Asteroids 3, 24, 60, 261, and 863. *Icarus* 77, 171–186.
- Hudson, S., 1993. Three-dimensional reconstruction of asteroids from radar observations. *Remote Sens. Rev.* 8, 195–203.
- Jacobson, S.A., Scheeres, D.J., 2011. Dynamics of rotationally fissioned asteroids: Source of observed small asteroid systems. *Icarus* 214, 161–178.
- Kušnirák, P., Pravec, P., Galád, A., Kornoš, L., Cooney, W., Gross, J., Terrell, D., 2008. 2005 NB7. *CBET* 1383.
- Magri, C. et al., 2007. Radar observations and a physical model of Asteroid 1580 Betulia. *Icarus* 186, 152–177.
- Margot, J.-L. et al., 2002a. Binary asteroids in the near-Earth object population. *Science* 296, 1445–1448.
- Margot, J.-L. et al., 2002b. Radar discovery and characterization of binary near-Earth asteroids. 33rd Annual Lunar and Planetary Science Conference, March 11–15, 2002, Houston, Texas. Abstract No. 1849.
- Margot, J.L. et al., 2003. 1937 UB (Hermes). *IAU Circ.* 8227.
- McMahon, J., Scheeres, D., 2010. Detailed prediction for the BYORP effect on binary near-Earth Asteroid (66391) 1999 KW4 and implications for the binary population. *Icarus* 209, 494–509.
- Mitchell, D.L., et al., 1996. Observations of Asteroids 1 Ceres, 2 Pallas, and 4 Vesta. *Icarus* 124, 113–133.
- Mottola, S., Hahn, G., Pravec, P., Sarounova, L., 1997. S/1997 (3671) 1. *IAU Circ.* 6680.
- Mueller, M. et al., 2011. ExploreNEOs. III. Physical characterization of 65 potential spacecraft target asteroids. *Astron. J.* 141, 109–117.
- Neish, C.D., Nolan, M.C., Howell, E.S., Rivkin, A.S., 2004. Radar observations of binary Asteroid 5381 Sekhmet. *Bull. Am. Astron. Soc.* 35, 1421.
- Nolan, M.C. et al., 2000. 2000 UG11. *IAU Circ.* 7518.
- Nolan, M.C. et al., 2002a. 2002 BM26. *IAU Circ.* 7824.
- Nolan, M.C. et al., 2002b. 2002 KK8. *IAU Circ.* 7921.
- Nolan, M.C., Hine, A.A., Howell, E.S., Benner, L.A.M., Giorgini, J.D., 2003. 2003 SS84. *IAU Circ.* 8220.
- Nolan, M.C., Howell, E.S., Miranda, G., 2004. Radar images of binary Asteroid 2003 YT1. *Bull. Am. Astron. Soc.* 36, 1132.
- Nolan, M.C. et al., 2008. Arecibo radar imaging of 2001 SN263: A near-Earth triple asteroid system. *Asteroids, Comets, Meteors* 2008, 8258.
- Ostro, S.J., Giorgini, J.D., 2004. The role of radar in predicting and preventing asteroid and comet collisions with Earth. In: Belton, M.J.S., Morgan, T.H., Samarasinha, N.H., Yeomans, D.K. (Eds.), *Mitigation of Hazardous Comets and Asteroids*. Cambridge Univ. Press, Cambridge, pp. 38–65.

- Ostro, S.J., Rosema, K.D., Campbell, D.B., Shapiro, I.I., 2002. Radar observations of Asteroid 1862 Apollo. *Icarus* 156, 580–583.
- Ostro, S.J., Nolan, M.C., Benner, L.A.M., Giorgini, J.D., Margot, J.L., Magri, C., 2003. 1990 OS. *IAU Circ.* 8237.
- Ostro, S.J. et al., 2005. (1862) Apollo. *IAU Circ.* 8627.
- Ostro, S.J. et al., 2006. Radar imaging of binary near-Earth Asteroid (66391) 1999 KW4. *Science* 314, 1276–1280.
- Pravec, P., Hahn, G., 1997. Two-period lightcurve of 1994 AW1: Indication of a binary asteroid? *Icarus* 127, 431–440.
- Pravec, P., Harris, A.W., 2000. Fast and slow rotation of asteroids. *Icarus* 148, 12–20.
- Pravec, P., Harris, A.W., 2007. Binary asteroid population. 1. Angular momentum content. *Icarus* 190, 250–259.
- Pravec, P., Wolf, M., Šarounová, L., 1998. Occultation/eclipse events in binary Asteroid 1991 VH. *Icarus* 133, 79–88.
- Pravec, P. et al., 2006. Photometric survey of binary near-Earth asteroids. *Icarus* 181, 63–93.
- Reddy, V. et al., 2006a. Photometric and radar observations of 2005 AB: A new binary near-Earth asteroid. *Lunar Planet. Sci.* XXXVII, 1755.
- Reddy, V. et al., 2006b. (7088) Ishtar. *CBET* 384.
- Scheeres, D.J., 2007. Rotational fission of contact binary asteroids. *Icarus* 189, 370–385.
- Shepard, M.K. et al., 2006. Radar and infrared observations of binary near-Earth Asteroid 2002 CE26. *Icarus* 184, 198–210.
- Shepard, M.K., Nolan, M.C., Benner, L.A.M., Giorgini, J.D., Ostro, S.J., Magri, C., 2008. 2005 NB7. *IAU Circ.* 8936.
- Taylor, P.A., Margot, J.L., 2010. Tidal evolution of close binary asteroid systems. *Celest. Mech. Dynam. Astron.* 108, 315–338.
- Taylor, P.A. et al., 2008. The shape, mutual orbit, and tidal evolution of binary near-Earth Asteroid 2004 DC. *Asteroids, Comets, Meteors 2008*, 8322.
- Taylor, P.A. et al., 2009. 2000 CO101. *CBET* 1957.
- Veeder, G.J., Hanner, M.S., Matson, D.L., Tedesco, E.F., Lebofsky, L.A., Tokunaga, A.T., 1989. Radiometry of near-Earth asteroids. *Astron. J.* 97, 1211–1219.
- Walsh, K.J., Richardson, D.C., Michel, P., 2008. Rotational breakup as the origin of small binary asteroids. *Nature* 454, 188–191.
- Wasson, J.T., 1974. *Meteorites: Classification and Properties*. Springer, New York, pp. 175–176.